



## Feasibility study for SOFC-GT hybrid locomotive power: Part I. Development of a dynamic 3.5 MW SOFC-GT FORTRAN model

Andrew S. Martinez, Jacob Brouwer\*, G. Scott Samuelsen

National Fuel Cell Research Center, University of California, Irvine, CA 92697-3550, USA

### ARTICLE INFO

#### Article history:

Received 21 January 2012

Received in revised form

10 April 2012

Accepted 12 April 2012

Available online 22 April 2012

#### Keywords:

SOFC-GT

Locomotive

Diesel

Feasibility

Dynamic Simulation

Cascade Control

### ABSTRACT

This work presents the development of a dynamic SOFC-GT hybrid system model applied to a long-haul freight locomotive in operation. Given the expectations of the rail industry, the model is used to develop a preliminary analysis of the proposed system's operational capability on conventional diesel fuel as well as natural gas and hydrogen as potential fuels in the future. It is found that operation of the system on all three of these fuels is feasible with favorable efficiencies and reasonable dynamic response. The use of diesel fuel reformat in the SOFC presents a challenge to the electrochemistry, especially as it relates to control and optimization of the fuel utilization in the anode compartment. This is found to arise from the large amount of carbon monoxide in diesel reformat that is fed to the fuel cell, limiting the maximum fuel utilization possible. This presents an opportunity for further investigations into carbon monoxide electrochemical oxidation and/or system integration studies where the efficiency of the fuel reformer can be balanced against the needs of the SOFC.

© 2012 Elsevier B.V. All rights reserved.

### 1. Introduction

Long-haul locomotive transportation is one of the most prevalent methods of shipping goods in the United States. An exploratory committee formed in 2002 at the Center for Transportation Research at Argonne National Laboratory, under the guidance of the U.S. Department of Energy, reported that in 1997, 4 billion gallons of diesel fuel were consumed by locomotives in the United States. This amount represents 10% of all diesel used for transportation and 2.3% of all transportation fuels. For the rail operators, this represents an annual cost of \$2 billion, contributing 7% of their total operating expenses [1]. Today, the situation is not much different, as the consumption of petroleum in freight rail represented 2.1% of the total national transportation fuel use in 2005, thereby consuming 571.4 trillion BTUs of fuel [2]. Thus, fuel use for long-haul locomotives is continually of economic interest to both government and industry, and represents a field with much potential for increasing energy independence.

In addition to these motivating factors, the use of diesel fuel in railway applications presents a significant environmental concern. Although the nationally averaged emission signature of locomotives

nationwide appears low (in 2001, locomotive-sourced  $\text{NO}_x$  was only 5% of the national total), locomotives are responsible for much of the emissions, especially diesel PM, in the areas where they are stationary [1]. At classification railyards, locomotives are responsible for 96% of PM emissions; at intermodal railyards, the contribution is 39% [3]. The general public living near these stationary rail operations is most affected by these emissions, and improvements in locomotive emission signatures can enhance the air quality for this subset of the population. Moreover, in California, rail operations tend to be centered in areas that have difficulty achieving air quality standards due to high source concentration and stagnating meteorological conditions; thus, the additional burden is placed on those living in areas already known to have poor air quality. Current estimates attribute 2980 premature deaths, 5100 cases of acute bronchitis, 62,000 cases of asthma and other respiratory problems, and 830 heart-related hospital admissions per year to goods movement in the Southern California Air Basin [4]. Similar to passenger vehicles and diesel freight trucks, locomotives have thus been assigned a progressively limiting tier-based schedule of emissions standards. This Tier system requires substantial ongoing reductions in the emission of  $\text{NO}_x$ , CO, hydrocarbons, smoke, and particulates [5].

Satisfying the ever-evolving Tier standards may require investigation of technology beyond the conventional combustion reciprocating engine. Early investment in emerging technologies, such as Solid Oxide Fuel Cells (SOFC), may provide more options

\* Corresponding author. Tel.: +1 9498241999; fax: +1 9498247423.  
E-mail address: [jb@nfrcc.uci.edu](mailto:jb@nfrcc.uci.edu) (J. Brouwer).

and enable development of systems with greater environmental benefit. The fuel cell has already been identified as having the capability to replace the entire diesel and electric power system for a locomotive, simply based on economic and performance concerns [1]. Moreover, the proven high efficiency and low emissions signature [6,7] of SOFC-based systems, for both criteria pollutants and greenhouse gases like CO<sub>2</sub>, present a compelling opportunity for vast improvement in the overall economic, environmental, and health impacts of freight railroading.

In spite of the fact that fuel cells in general have been considered in the literature for the freight locomotive application, very little work has been presented for the use of the solid oxide fuel cell in particular. Most theoretical studies and the only major demonstration project to-date have focused on utilizing low-temperature proton exchange membrane (PEM) fuel cells [8–14]. Systems assuming on-board power, off-board power with electrified line, and hybridization with large auxiliary battery storage have been investigated [9,11–14]. The last of these is the subject of a substantial demonstration project in the United States as part of a collaborative effort between the Burlington Northern Santa Fe Railway System and Vehicle Projects, LLC [15–17].

Although the PEM systems have shown promise, their operation requires a hydrogen infrastructure, a constraint that may be too limiting at the moment for widespread adoption and which the SOFC can avoid thanks to its fuel-flexible operation. Additionally, the SOFC can be hybridized with a gas turbine (termed an SOFC-GT), allowing for a number of synergistic benefits. Such a system has been shown to potentially operate at efficiencies above 60%, produce virtually zero levels of criteria pollutants, and operate with low noise levels due to the small number of moving parts. The ability to accomplish all of these and operate on the currently used diesel fuel is a capability that is unique to the combination of high-temperature fuel cell with gas turbine.

Since the introduction of the SOFC-GT concept, there has been significant advancement in understanding prototypical systems through work simulating the performance of various designs and exploring detailed considerations such as system integration, control optimization, and drivers and challenges in the expected dynamic response [18–27]. In addition, the available literature is rich with a variety of study methodologies and system design options to develop in-depth understanding of key system-wide dynamic interactions and component limitations as well as identification of preferred system designs. Finally, the SOFC-GT research community has also been able to demonstrate the potential of these systems to be flexible in application, through analyses of systems applied to such varied goals as grid stabilization, Integrated Coal Gasification-Fuel Cell plants, and Distributed Energy Resources [28–30].

However, these prior research works are all based on the designs of SOFC-GT systems for stationary power. With its high fuel-to-electric conversion efficiency, the SOFC-GT is an ideal candidate for stationary power applications, especially large-scale and centralized power. This feature is also attractive in the locomotive application, since the wheels are run by electric traction motors. Still, the combination of the SOFC-GT with this mobile platform has yet to make an appearance in the literature. Mobile SOFC-GT systems have been proposed by Winkler and Lorenz, but for the smaller passenger vehicle platform [31]. There is also some available literature regarding the application of SOFC-GT systems for marine applications [32,33]. As of the time of this publication, there does not seem to be any investigation of the potential for the SOFC-GT hybrid system for the locomotive application.

Significant capital investment in new fueling infrastructure required by PEM solutions can be avoided by taking advantage of the SOFC-GT fuel flexibility. This study has adopted a scenario in

which diesel fuel is the near-term choice, followed by natural gas as a bridging fuel, and finally hydrogen as an end-goal fuel in the future. It is assumed that the two fossil fuels are pre-reformed off board from the locomotive. Thus, this work analyzes the performance of the system when operated on a diesel autothermal reformate, a natural gas steam methane reformate, and humidified hydrogen. Possibilities for on-board reformation will be the subject of future work.

To develop the model, this work builds upon the foundation laid out by the previous studies and aims to provide insight into the unique issues of the SOFC-GT in a large mobile platform. The major issues include the need for fuel processing to accommodate diesel fuel use and the prediction of SOFC degradation due to coke development in the anode. For this reason, the current investigation develops a model of an SOFC-GT system that operates on hydrogen or fuel reformates, but is flexible enough to later incorporate the requirements of the reformer and the undesired but prevalent effects of coking reactions. Because these chemical processes are often complex and include reactions on vastly different timescales, the model was developed with flexible control over numerical algorithms specifically designed for the solution of stiff ODEs in concert with simulation of the remaining pertinent physics in the fuel cell.

Therefore, a novel model framework was developed and implemented in FORTRAN, which leaves open the possibility of incorporation of various numerical schemes for reaction chemistry necessary for investigating the dependency of system performance on fuel choice. In addition, since future versions of the model are projected to incorporate a voltage loss mechanism based on the simulation of coking deposition within the fuel cell, the method of convergence for the current-voltage relationship has been designed to accommodate for more than just the traditional loss mechanisms, which often allows for simplifications in the SOFC model development. This paper presents the development of this model and insights into steady-state fuel dependence.

## 2. Modeling methodology

### 2.1. Global solution method

The FORTRAN model developed in this work consisted of a set of modular subsystems based on the analysis of each major component in the system. Each subsystem required iteration to convergence within itself, and in some cases required repeated convergence iteration among subsystems. The schematic of the system modeled in this work is as shown in Fig. 1. It is a simplified model of the extensive system expected to be required of an SOFC-GT powering a locomotive and includes the major components and features required in this application. Namely, the system includes direct linking between the SOFC and gas turbine units, includes an auxiliary combustor before the turbine, includes an air preheater supported by system waste heat, and includes cathode recycle to aid SOFC thermal management. Some balance of plant components are not accounted for in this model (such as fuel pumps, a fuel preheater, and any necessary fuel processing equipment); thus, the performance found in this investigation will be slightly improved compared to a more detailed system model. It is expected that this simplification still provides a reasonable expectation of the system's capabilities.

The overall system model is divided into four major subsystems: the SOFC subsystem, the gas turbine subsystem, the air preheater subsystem, and the controller. The first three of these are closely tied via fluid streams passing through all of these subsystems. Thus, convergence within each subsystem must be matched by global convergence of values shared between subsystems. In order to

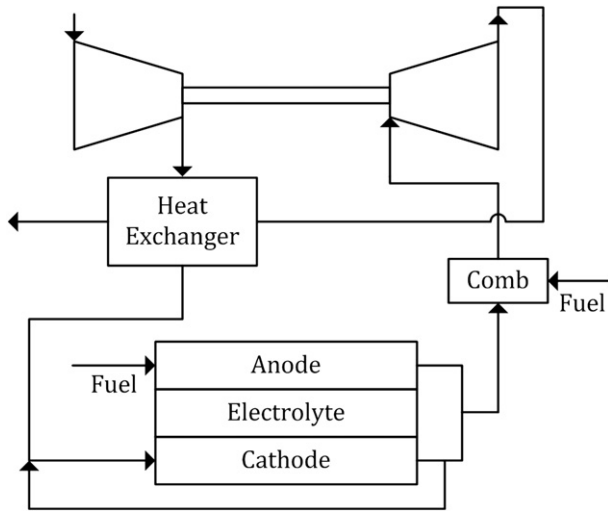


Fig. 1. Base SOFC-GT system simulated and analyzed in this work.

achieve this, the gas turbine subsystem was chosen for the overall convergence check. Given the shaft speed and pressure ratio utilized for interpolation on the compressor performance map, the turbine model calculated an expected mass flowrate based on similar interpolation. Agreement between this flowrate and the flowrate leaving the combustor determined overall system convergence. Within the air preheater and the SOFC, internal convergence criteria determined the gas and component states for a given global pair of gas turbine shaft speed and pressure ratio. If global system convergence was not obtained, the pressure ratio was adjusted and all subsystems reevaluated. In order to close the solution at the air preheater, the current timestep air from the compressor and previous timestep exhaust from the turbine were utilized. Accuracy was maintained due to the small timesteps utilized in this investigation.

## 2.2. SOFC subsystem model

The solid oxide fuel cell subsystem is based on a quasi two-dimensional dynamic model, with spatial resolution along the flow path of the anode and cathode gases for a single fuel cell. It is assumed in the model that the anode and cathode flows are arranged in a co-flow orientation. An entire fuel cell stack is assumed to be comprised of multiple cells, each of which has multiple channels with the same conditions as those solved for by the fuel cell module. This simplification is illustrated in Fig. 2, depicting the reduction from a stack of cells to a representative central cell, and further to a representative central channel pair (anode and cathode) with associated solid structures (fuel cell tri-layer and current collector). Finally, in order to achieve spatial resolution in the model, this representative geometry is then subdivided along its flow direction into nodes. In this work, each channel was simulated with 10 nodes; the total area of the simulated square cell was  $0.25 \text{ m}^2$ . Each node contained four control volumes: anode gas, cathode gas, tri-layer, and current collector. In addition, given the small length and timescales of the simulation, each node was assumed to behave similar to an individual perfectly stirred reactor. This allows each node in the channel to be solved sequentially, with the state of a given node acting as the inlet of the next node.

The SOFC nodes are each solved in the same manner, through the completion of five major processes: the thermodynamics, conservation of momentum, reaction kinetics, electrochemistry and conservation of mass, and heat transfer processes. The organization and sequential implementation of these processes within each node is shown in Fig. 3. These processes cumulatively represent the fundamental conservations of mass, momentum, energy, and charge. The division into the separate processes allows the solution of the ensemble effect of a number of interacting physics via consideration of one physical operator at a time, with iteration allowing for coordinated solution amongst the operators. This is achieved by evaluation of the thermodynamics process, which

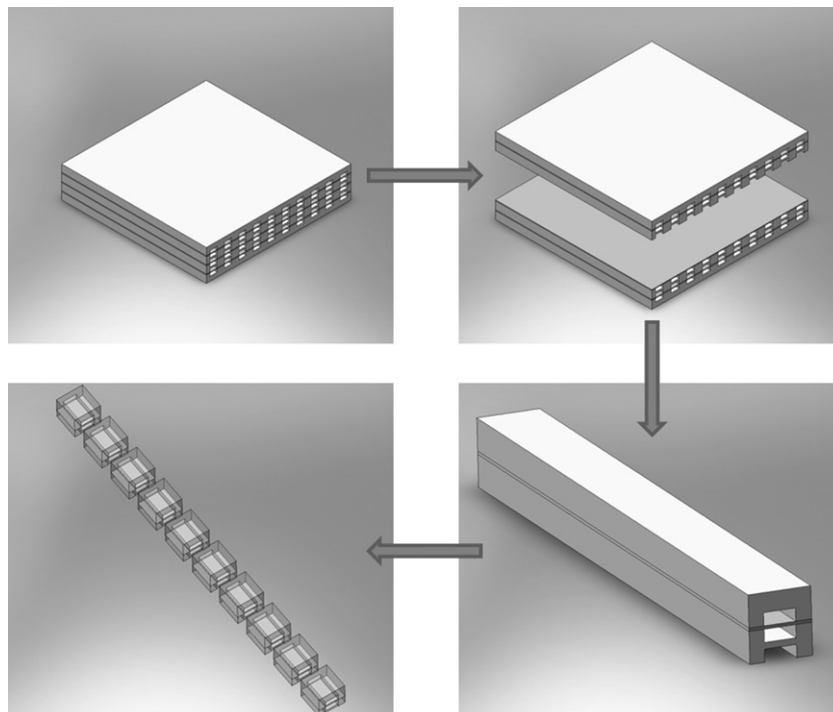


Fig. 2. Sequential simplification from SOFC stack to model channel-based domain.

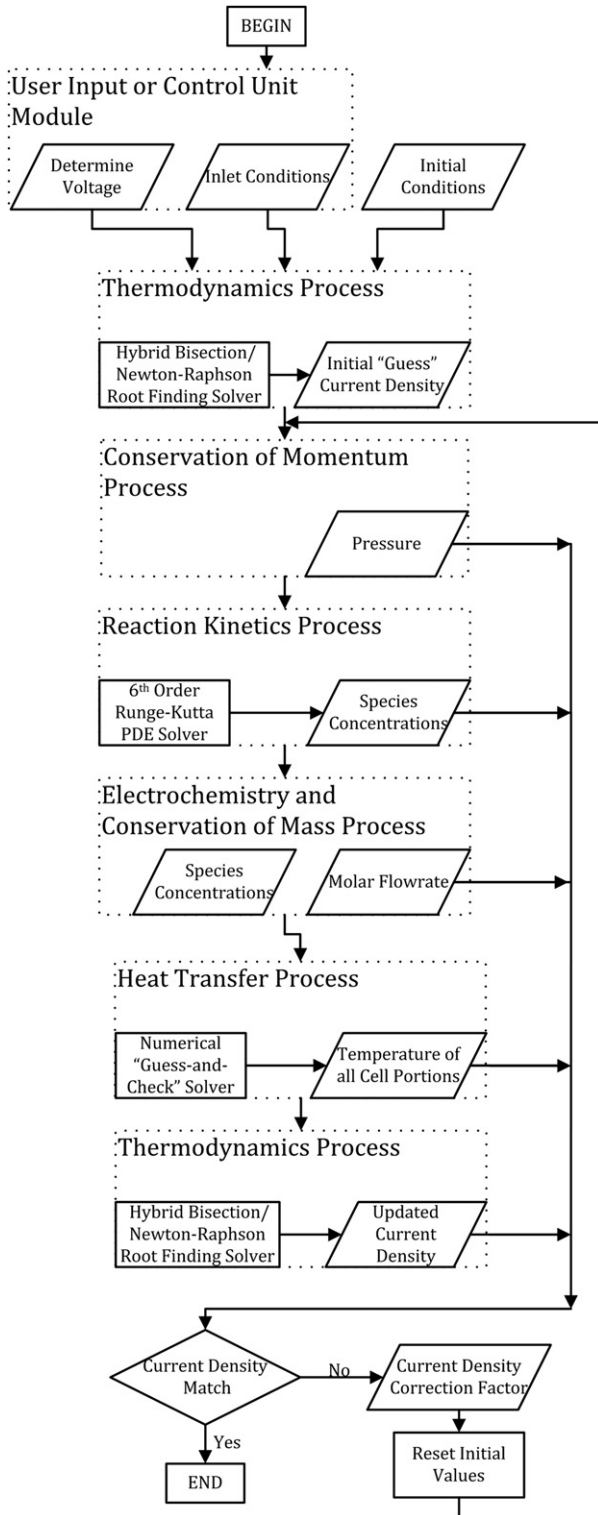


Fig. 3. SOFC subsystem process flow and convergence.

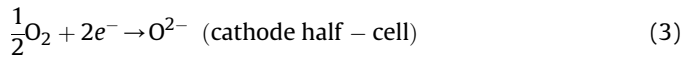
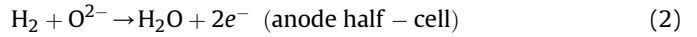
calculates current density as its output, as the first and last step of the operator sequence. Convergence was then dictated by a match between the current density in the first and second call to the thermodynamics process.

The thermodynamics process utilizes standard expressions of voltage related to current density and electrochemical losses modeled after the work of Costamagna et al. [34]. The output of this

process was the current density based on a set of given conditions within the node and the voltage passed to the process from the system controller. Current density was calculated implicitly through evaluation of the cell voltage via the modeled overpotential terms:

$$E_1 = E_N - \eta_{\text{Activation,A}} - \eta_{\text{Activation,C}} - \eta_{\text{Concentration,A}} - \eta_{\text{Concentration,C}} - \eta_{\text{Ohmic}} \quad (1)$$

where  $E_1$  is the cell voltage,  $E_N$  is the Nernst potential, and the various  $\eta$  represent the anode and cathode activation and concentration overpotentials and the cell overall ohmic overpotential. Since hydrogen was assumed to be the only electrochemically active fuel in the cell, the reactions in each half-cell are represented by



and the associated change in Gibbs' Free Energy for the reaction defined as

$$\Delta g_{\text{rxn}} = \Delta h_{\text{rxn}} - T_{\text{Tri}} \Delta s_{\text{rxn}} \quad (4)$$

where

$$\Delta h_{\text{rxn}} = h_{\text{H}_2\text{O}}(T_{\text{Tri}}) - \frac{1}{2}h_{\text{O}_2}(T_{\text{Tri}}) - h_{\text{H}_2}(T_{\text{Tri}}) \quad (5)$$

$$\Delta s_{\text{rxn}} = s_{\text{H}_2\text{O}}(T_{\text{Tri}}) - \frac{1}{2}s_{\text{O}_2}(T_{\text{Tri}}) - s_{\text{H}_2}(T_{\text{Tri}}) \quad (6)$$

The Nernst potential can then be expressed as

$$E_N = E_0 + \frac{RT_{\text{Tri}}}{nF} \ln \left( \frac{p_{\text{H}_2} \cdot p_{\text{O}_2}^{1/2}}{p_{\text{H}_2\text{O}}} \right) \quad (7)$$

where

$$E_0 = \frac{-\Delta g_{\text{rxn}}}{nF} \quad (8)$$

where  $T_{\text{Tri}}$  is tri-layer temperature,  $p_i$  is the partial pressure of component  $i$ ,  $n$  is the number of electrons participating in the reaction (in this case 2), and  $F$  is Faraday's constant.

The definitions for the loss terms themselves followed the formulation presented in Costamagna et al. with two notable exceptions. In the current model, the activation polarization is defined separately for each electrode according to an arcsinh approximation:

$$\eta_{\text{Activation},i} = \frac{RT_{\text{Tri}}}{\alpha nF} \cdot \sinh^{-1} \left( \frac{j}{2j_{0,i}} \right) \quad (9)$$

where  $j$  is current density and  $\alpha$  is the reaction's symmetry factor, assumed to be 0.5. The calculation of the exchange current density,  $j_{0,i}$ , was the same as the previous work. In addition, the definition of the area-specific resistance (ASR) was simplified from the previous work, which included multiple factors for the unique shape of the particular SOFC unit modeled. In the current work, ASR was simply defined as

$$\text{ASR} = \rho_A d_A + \rho_C d_C + \rho_{\text{Elec}} d_{\text{Elec}} + \rho_{\text{CC}} d_{\text{CC,A}} + \rho_{\text{CC}} d_{\text{CC,C}} \quad (10)$$

where  $\rho$  denotes resistivity of the various materials and  $d$  represents their thicknesses. The values of the resistivities of all

**Table 1**  
Arrhenius equation constants for modeled reformation reactions.

Reaction	A	E <sub>a</sub> (kJ·mol <sup>-1</sup> )
CH <sub>4</sub> + H <sub>2</sub> O ↔ CO + 3H <sub>2</sub>	6.043e15	240.1
CO + H <sub>2</sub> O ↔ CO <sub>2</sub> + H <sub>2</sub>	1.28e6	67.13
CH <sub>4</sub> + 2H <sub>2</sub> O ↔ CO <sub>2</sub> + 4H <sub>2</sub>	1.459e15	243.9

materials except for the cathode were modeled as temperature-dependent, again following the values formulated in [34]. The current work assumes an anode-supported cell; thus, the thicknesses modeled in this work were as follows:

$$d_A = 210 \text{ } \mu\text{m}, \quad d_C = 30 \text{ } \mu\text{m}, \quad d_{\text{Elec}} = 10 \text{ } \mu\text{m}, \\ d_{\text{CC,A}} = 125 \text{ } \mu\text{m}, \quad d_{\text{CC,C}} = 125 \text{ } \mu\text{m}$$

The conservation of momentum process calculated the pressure drop in each flow channel via

$$\Delta P = \frac{\rho V^2 f}{2D_H} \Delta x \quad (11)$$

where  $\Delta P$  is the pressure drop,  $\rho$  is the mixture density,  $V$  is the flow velocity,  $D_H$  is the channel hydraulic diameter, and  $\Delta x$  is the node length. Gas channel height and width were assumed to be 1 mm and 3 mm, respectively. The flow was assumed to be laminar; thus, the friction factor was

$$f = \frac{64}{Re} \quad (12)$$

where  $Re$  is the flow Reynolds number.

The reaction kinetics process determined changes in species concentrations due to the action of reformation reactions and water–gas shift chemistry. In the current model, only three reactions were assumed to take place. The reactions and their rate parameters according to the Arrhenius equation are described in Table 1. These model reactions are not the elementary reactions expected to occur within the cell; rather, they are summary reactions that represent the global effect of a much larger number of elementary homogeneous and heterogeneous reactions taking place in the channel and interacting with the nickel in the anode, respectively. Rate data was obtained from a pilot investigation utilizing Chemkin, which resulted in values slightly altered from those reported in [6], after which the reformation reactions were modeled. In addition, all reaction rates were inversely scaled by an adsorption rate constant described by Eq. (13), with  $y_x$  representing the mole fraction of species  $x$  and the values listed in Table 2.

$$\text{DEN} = \left( 1 + k_{\text{ads,CO}} \cdot y_{\text{CO}} + k_{\text{ads,H}_2} \cdot y_{\text{H}_2} + k_{\text{ads,CH}_4} \cdot y_{\text{CH}_4} + k_{\text{ads,H}_2\text{O}} \cdot \frac{y_{\text{H}_2\text{O}}}{y_{\text{H}_2}} \right)^2 \quad (13)$$

The overall effect of the DEN term is simply to provide a mechanism of accounting for the slower adsorption kinetics on the Ni surface as compared to the kinetics of the reformation reactions.

The electrochemistry and conservation of mass process simulates the transfer of the oxygen ions from the cathode flow channel

**Table 2**  
Adsorption rate constants utilized in Eq. (13).

Reaction rate	A	E <sub>a</sub> (kJ·mol <sup>-1</sup> )
$k_{\text{ads,CO}}$	6.12e-9	-82.9
$k_{\text{ads,H}_2}$	6.65e4	-38.28
$k_{\text{ads,CH}_4}$	1.77e5	88.68
$k_{\text{ads,H}_2\text{O}}$	8.230e-5	-70.65

to the anode flow channel, thereby determining the change in species concentrations and total molar and mass flowrate in both channels. In the current model, it is assumed that hydrogen is the only fuel species participating in electrochemical oxidation on the anode side; the effect of this assumption will be discussed further below. Under this assumption, the reactions occurring in the two flow control volumes are as specified in Eqs. (2) and (3). Extension of Faraday's Law to a balance of molar flow within each channel then dictates that the output mole fractions of all participating species, after electrochemistry, are described by

$$y_{\text{H}_2,\text{Anode}} = \frac{\dot{N}_{\text{Inlet,A}} y_{\text{H}_2,\text{A,Inlet}} - \dot{N}_{\text{ion}}}{\dot{N}_{\text{Inlet,A}}} \quad (14)$$

$$y_{\text{H}_2\text{O},\text{Anode}} = \frac{\dot{N}_{\text{Inlet,A}} y_{\text{H}_2\text{O},\text{A,Inlet}} - \dot{N}_{\text{ion}}}{\dot{N}_{\text{Inlet,A}}} \quad (15)$$

$$y_{\text{O}_2,\text{Cathode}} = \frac{\dot{N}_{\text{C,Inlet}} y_{\text{O}_2,\text{C,Inlet}} - 0.5 \cdot \dot{N}_{\text{ion}}}{\dot{N}_{\text{C}}} \quad (16)$$

$$y_{\text{N}_2,\text{Cathode}} = \frac{\dot{N}_{\text{C,Inlet}} y_{\text{N}_2,\text{C,Inlet}}}{\dot{N}_{\text{C}}} \quad (17)$$

where  $\dot{N}$  represents the molar flowrate, and  $\dot{N}_{\text{ion}}$  represents a source on the anode and a sink on the cathode side, determined via:

$$\dot{N}_{\text{ion}} = \frac{I}{2F} \quad (18)$$

$$\dot{N}_{\text{C}} = \dot{N}_{\text{Inlet,C}} - 0.5 \cdot \dot{N}_{\text{ion}} \quad (19)$$

Finally, the heat transfer process determines the temperatures of all four control volumes within the SOFC node. Since four temperatures must be determined, and all are dependent on each other, the solution method for this process was a guess-and-check method, similar to the overall SOFC subsystem. Convergence was determined to occur when the temperatures in all four control volumes were such that energy conservation could be satisfied. Three general categories of thermal energy exchanges were accounted for in this model: convective heat transfers, conductive heat transfers, and thermal energy sources and sinks.

Convective transfers included transfers between the anode and cathode flow channels and both the tri-layer and current conductor control volumes. In addition, mass flows that advected thermal energy through the system were accounted for; these included thermal energy entering and exiting the anode and cathode control volumes through gas flow and the thermal energy carried by the oxygen ion modeled as leaving the cathode gas flow, entering the tri-layer, experiencing a near-instantaneous change in temperature to the tri-layer temperature, and finally exiting the tri-layer to enter the anode gas. According to the perfectly stirred reactor assumptions, all thermal energy exiting the flow control volumes was modeled at the converged temperature of the control volume within the node. For the convective transfers between gaseous and solid control volumes, the convective heat transfer coefficient was modeled as

$$h_i = \frac{Nu_j \cdot k_i}{D_{H,j}} \quad (20)$$

where  $Nu_j$  is the Nusselt number correlation given the non-circular geometry of the channel as well as the aspect ratio of the channel,

$D_{H,i}$  is the hydraulic diameter of gas channel  $j$ , and  $k_i$  is the thermal conductivity of gas phase  $i$ . The correlation for  $Nu_i$  used in the simulation was based on empirical data provided in [35].

Conductive heat transfers were only modeled in the solid phases between adjacent nodes of the same control volume and also between the current collector and tri-layer control volumes within a given node. In general, the conduction between adjacent nodes of the same control volume was modeled as

$$E_{\text{Condi},i-1} = \frac{kA_{X-\text{Sec}}(T_i - T_{i-1})}{dx} \cdot dt, E_{\text{Condi},i+1} = \frac{kA_{X-\text{Sec}}(T_i - T_{i+1})}{dx} \cdot dt \quad (21)$$

where  $i$  is the index of the current node,  $k$  is the thermal conductivity of the given material,  $A_{X-\text{Sec}}$  is the cross-sectional area through which the energy is transferred, and  $T$  is the temperature at the indicated node. Conduction between the current conductor and the tri-layer in a given node was modeled as

$$E_{\text{Condi},T \rightarrow \text{CC}} = \frac{k_{\text{Avg,H}}A_{\text{CC-T}}(T_{\text{Tri}} - T_{\text{CC}})}{dy} \cdot dt \quad (22)$$

where  $k_{\text{Avg,H}}$  is the harmonic average of the two materials' thermal conductivities,  $A_{\text{CC-T}}$  is the area of contact between the current collector and tri-layer,  $T$  is the temperature, and  $dy$  is the distance from the center of the current collector to the center of the tri-layer, in the direction of travel of the heat exchange (e.g. through the thickness of these two phases).

All thermal sources in the model originated from the action of electrochemistry within the cell. All of these thermal sources were modeled to exist within the tri-layer, as they originate from the action of the electrolyte and electrodes. Therefore, the calculation for all the electrochemical losses' energy contents,  $E_{\text{Act,A}}$ ,  $E_{\text{Act,C}}$ ,  $E_{\text{Cnc,A}}$ ,  $E_{\text{Cnc,C}}$ , and  $E_{\text{Ohm}}$  were derived from their analogs presented earlier. The electrical energy leaving the node to the external circuit was the only sink and taken simply as

$$E_{\text{Elec}} = IV \cdot dt \quad (23)$$

where  $I$  is the current and  $V$  is the voltage. The final energy source was the entropic loss experienced at the standard potential, calculated as

$$E_{\text{Entropy}} = \Delta S_{\text{rxn}} \dot{N}_{\text{ion}} T_{\text{Tri}} \cdot dt \quad (24)$$

### 2.3. Gas turbine subsystem model

The gas turbine subsystem utilizes compressor and turbine performance maps to determine the turbomachinery's state at each timestep. Convergence across this subsystem is determined by satisfaction of mass balance across the gas turbine, with the map's predicted mass flowrate required to match that exiting the auxiliary combustor. The compressor and turbine maps themselves were modified versions of generalized performance maps readily available from the freeware GasTurb 11. The compressor and turbine maps were scaled to values that represent the reported design point performance of the Solar Turbines Saturn 20 gas turbine generator [36]. This particular turbine was chosen based on a preliminary study that determined its power (1.2 MW) and size (9.02 m<sup>2</sup>, 21.74 m<sup>3</sup>) were well-matched to the requirements of the hybrid system needed in this application; this development is presented in more detail in Part II of this work.

Interpolation was based on the shaft speed at the given timestep and guessed pressure ratio. With these two metrics known, it was possible to then use the maps to determine the isentropic efficiency and mass flowrate of the compressor and turbine. Map data in

GasTurb is provided along "β-lines," which give sets of mass flow, pressure ratio, and efficiency data at various shaft speeds along specified linear trends in the maps. Fig. 4 gives an example for the compressor map; solid lines are β-lines and dashed lines are lines of constant shaft speed. Similar relationships exist between the other performance variables and for the turbine performance as well. Determination of state was then a matter of locating the β-lines that bound the current state based on pressure ratio and shaft speed and then interpolating between these lines for mass flowrate and efficiency.

The only portion of the turbomachinery performance that was not determined from the maps was the shaft speed. This was determined by a torque balance on the shaft, which was itself controlled by the load demanded of the turbomachinery. Determination of the shaft speed followed

$$\frac{\partial N_{\text{GT}}}{\partial t} = \frac{1}{J_{\text{Shaft}} \cdot N_{\text{GT}}} \cdot (P_{\text{T}} - P_{\text{C}} - P_{\text{Load}} - P_{\text{Loss}}) \quad (25)$$

where  $P_{\text{T}}$ ,  $P_{\text{C}}$ ,  $P_{\text{Load}}$ , and  $P_{\text{Loss}}$  are the power generated by the turbine and the power consumed by the compressor, load, and losses, respectively.  $J_{\text{Shaft}}$  is the shaft's rotational inertia. The loss term was consistently set to 5% of the net difference between turbine and compressor power. This same relationship was used in the SOFC average temperature control's feed-forward portion to predict the load change required for a desired change in shaft speed.

Finally, the auxiliary combustor was also treated as part of the gas turbine subsystem. The auxiliary combustor accepted as input the depleted anode fuel stream, the portion of the cathode stream not recirculated, and a control signal for additional fuel flow. It was assumed that complete oxidation occurred within the combustor. Outlet species concentrations and temperatures were then calculated based on these parameters.

### 2.4. Air preheater subsystem model

The structure of the Air preheater subsystem was very similar to the SOFC; the heat exchanger was assumed to be a plate-and-fin type in counter-flow and only a single, centrally-located channel in the plate-and-fin array was modeled, with spatial resolution in the flow direction. As with the fuel cell, energy conservation was maintained in each individual control volume (fresh air, exhaust products, and solid) in order to determine convergence of the solution of all three temperatures simultaneously. Determination of

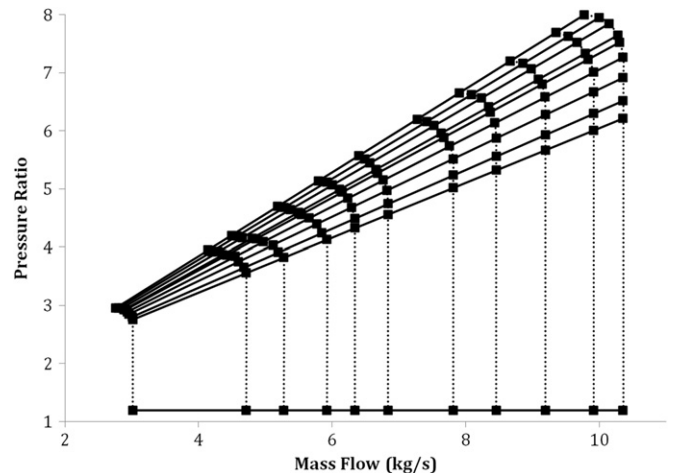


Fig. 4. Sample compressor map; solid lines are "β-lines", dotted lines are at constant shaft speed.

the convective heat transfer between the solid ( $S$ ) and a gas flow,  $i$ , followed [35], namely

$$E_{\text{Conv},S \rightarrow i} = h_{0,i} \cdot (A_{\text{Plate}} + A_{\text{Fin}}) \cdot \eta_{\text{Fin}} \cdot (T_{\text{Solid}} - T_{\text{Gas}}) \quad (26)$$

where  $\eta_{\text{Fin}}$  is the fin effectiveness, defined as

$$\eta_{\text{Fin}} = 1 - \left(1 - \eta_{\text{Fin}}^*\right) \cdot \frac{A_{\text{Fin}}}{A_{\text{Fin}} + A_{\text{Plate}}} \quad (27)$$

where

$$\eta_{\text{Fin}}^* = \frac{\tanh(m_i \cdot L_{\text{Fin}})}{m_i \cdot L_{\text{Fin}}} \quad (28)$$

$$m_i = \sqrt{\frac{h_{0,i} \cdot P}{k_{\text{Sol}} \cdot A_{X-\text{Sec},\text{Fin}}}} \quad (29)$$

$$L_{\text{Fin}} = H_{\text{Chan}} + W_{\text{Fin}} \quad (30)$$

where  $P$  is the perimeter of the fin's cross section,  $k_{\text{Sol}}$  is the conductive heat transfer coefficient for the fin's material,  $A_{X-\text{Sec},\text{Fin}}$  is the cross-sectional area of the fin,  $H_{\text{Chan}}$  is the height of the gas flow channel, and  $W_{\text{Fin}}$  is the thickness of the fin.

Given that the heat exchanger was modeled as counter-flow, and heat transfer was the only physics of interest within this subsystem, a faster solution scheme was utilized than the SOFC guess-and-check method. The effectiveness-NTU method was instead implemented. An overall heat transfer coefficient was defined as

$$UA = \frac{1}{\frac{1}{E_{\text{Conv},S \rightarrow C}} + \frac{1}{E_{\text{Conv},S \rightarrow H}}} \quad (31)$$

where  $E_{\text{Conv},S \rightarrow C}$  and  $E_{\text{Conv},S \rightarrow H}$  are the convective heat transfers on the cold and hot sides, respectively, following Eq. (26). The net transfer units (NTU) was then defined as

$$\text{NTU} = \frac{UA}{C_{\text{HR},\text{Min}}} \quad (32)$$

where  $C_{\text{HR},\text{Min}}$  is the smaller heat rate from between the hot and cold sides, defined as

$$C_{\text{HR}} = \sum_{i=1}^N C_{p,i}(T) \cdot \dot{N}_i \quad (33)$$

In addition, the ratio of the heat rates was defined as

$$R_{\text{HR}} = \frac{C_{\text{HR},\text{Min}}}{C_{\text{HR},\text{Max}}} \quad (34)$$

The effectiveness of heat transfer within a node could then be calculated from the above parameters according to

$$\epsilon = \frac{1 - \exp(-\text{NTU} \cdot (1 - R_{\text{HR}}))}{1 - R_{\text{HR}} \cdot \exp(-\text{NTU} \cdot (1 - R_{\text{HR}}))} \quad (35)$$

where all variables are as previously defined. Utilizing this effectiveness, the energy balance around an individual node's cold-side control volume would then be

$$\Delta E_{\text{Gas},C} = \epsilon \cdot (C_{\text{HR},\text{Min}} \cdot (T_{\text{Inlet},H} - T_{\text{Inlet},C})) - H_{\text{Outlet},C} + H_{\text{Inlet},C} \quad (36)$$

A similar balance could also be written for the hot side, but where the convective heat transfer is out of, instead of into, the control

volume. These balances were then solved iteratively for both channels, after which the balance for the solid phase was evaluated algebraically.

## 2.5. Control methodology

The control unit for the SOFC-GT hybrid system was designed to prioritize safe operation of the SOFC before attempting to satisfy system power requirements. In order to accomplish this, a cascade controller was implemented, with the structure shown in Fig. 5. In the SOFC, the major safety concern regards thermal stresses, induced by large temperature gradients and/or high operating temperature, which can cause fracture and potentially leaks of fuel gas. Thus, the two highest levels in the cascade ensure safe operation is achieved first, with average temperature controlled by the load on the turbine shaft (which will affect the system air flow) and temperature rise controlled by the relative amount of depleted air recirculated on the cathode side. Efficient SOFC operation was then moderated by controlling anode utilization via manipulation of the SOFC voltage. Finally, at the lowest priority, efficient turbine operation and satisfaction of system power demand were implemented. The former was achieved by controlling turbine inlet temperature through manipulation of the auxiliary fuel flow; the latter was achieved by manipulating the main system fuel flow, which occurs at the SOFC anode. Prioritization was implemented by setting bands in the controlled variable's state of "safe" or "preferred" operation, outside of which control was not allowed to proceed to a lower level. When necessary, an additional target setpoint value was specified. These specifications are provided in Table 3.

The majority of the control was achieved through proportional feedback control. The system net power was the only parameter observed to have a steady-state error under P-type only control; therefore, integral control was implemented in this instance. In addition, the SOFC average temperature control utilized a feed-forward signal to achieve greater stability. The physical parameter with the largest direct effect on the SOFC temperature is the flowrate of air through the cathode, which is dictated by the performance of the turbomachinery. In a physical system with variable shaft speed, air flowrate can be controlled by the application of load on the shaft, as indicated in the torque balance of Eq. (25). Thus, in order to implement the predictive capability required by feed-forward control, the change in required flowrate in the cathode would need to be translated into a change in load on the shaft.

This calculation process is embodied in Eqs. (37)–(39), followed by inversion of Eq. (25) to solve for load as a function of shaft speed. In order to predict the necessary air flow, the heat load generated by the cell must first be calculated, per Eq. (37) where  $P_{\text{Max}}$  is the maximum theoretical power (based on Nernst potential) at the converged current density. This heat load is assumed to be the primary forcing of the temperature rise along the cell length; thus, to maintain a desired temperature difference, an equal amount of heat with an equal temperature rise would need to be absorbed by the air flow in the cathode (it is implicitly assumed that the flow in the anode provides significantly less convective flux). Eq. (38) then provides an approximation for the air flowrate required.  $\Delta T_{\text{set}}$  is the maximum allowable temperature difference along the SOFC channel's length (200 K), and  $C_{p,\text{Ave}}$  is the specific heat of air at the converged average SOFC temperature. Finally, from the data supplied with the compressor map, an approximate relationship between shaft speed and air flowrate was developed as shown in Eq. (39), derived from a linear regression of the average relationship across all  $\beta$ -line data provided.

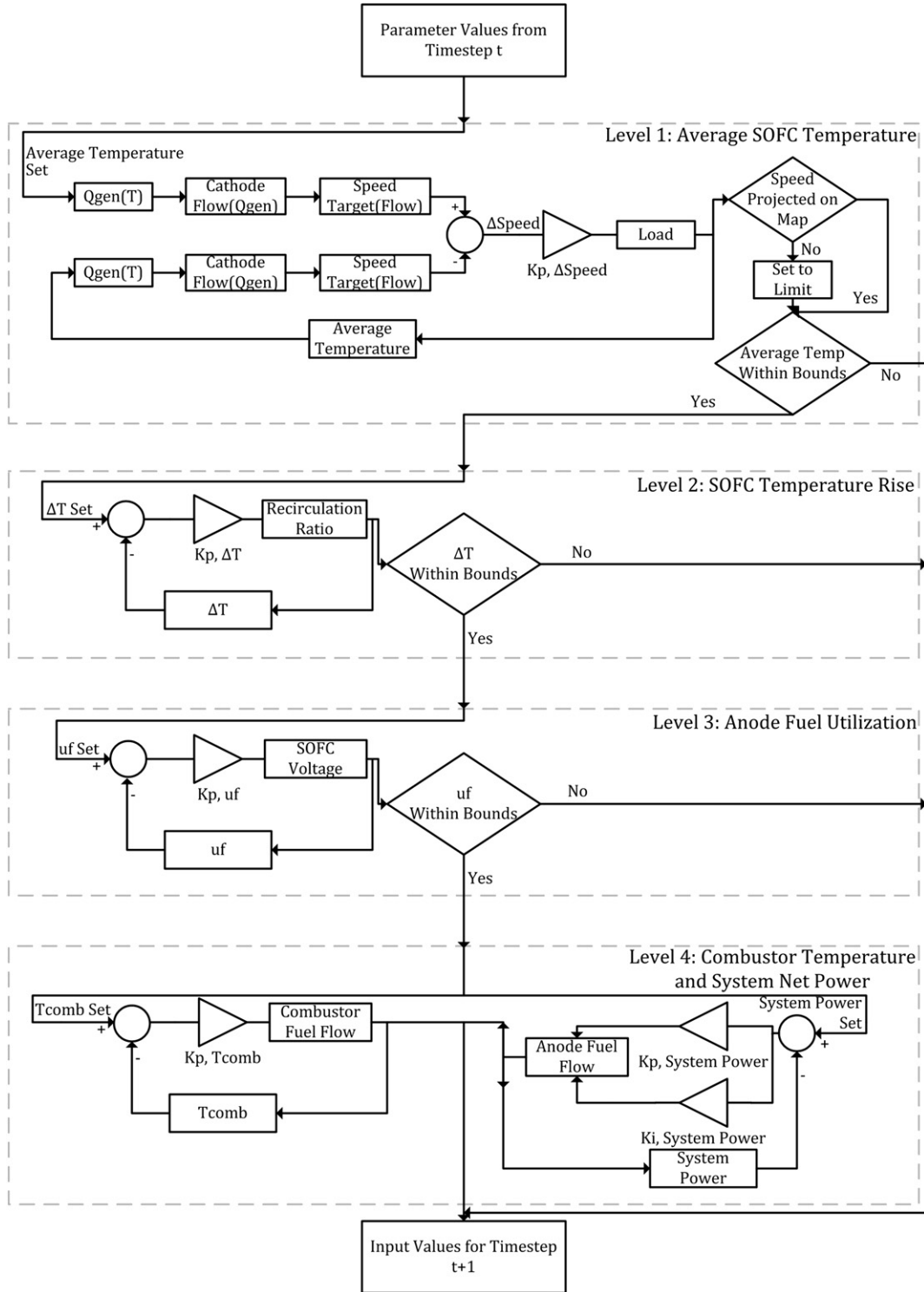


Fig. 5. Cascade controller logic.

$$Q_{\text{Gen}} = (P_{\text{Max}} - P_{\text{SOFC}}) \cdot N_{\text{Cell}} \quad (37)$$

$$\dot{M}_{\text{Air}} = \frac{Q_{\text{Gen}}}{\frac{C_{p,\text{Ave}}}{\text{MW}_{\text{Air}}} \cdot \Delta T_{\text{Set}}} \quad (38)$$

$$N_{\text{GT}} = 503.3 \cdot \dot{M}_{\text{Air}} + 9880.2 \quad (39)$$

### 3. System modeling results and discussion

#### 3.1. SOFC subsystem validation

Prior to integrating the SOFC Subsystem with the remainder of the model code, this module was validated against readily available data from a 1996 IEA project report [37]. In this report, several modeling efforts were discussed and various SOFC operating parameters provided for humidified hydrogen (90% H<sub>2</sub>; 10% H<sub>2</sub>O)



**Table 3**  
Controller targets and permissible operation bands.

Controlled parameter	Minimum value	Maximum value	Setpoint value
Average SOFC temperature	1067 K	1179 K	1123 K
SOFC temperature rise	–/–	200 K	–/–
Anode fuel utilization	0.7	0.9	0.85
Combustor/turbine inlet temperature	1223 K	1523 K	–/–
Total system net power	–/–	–/–	Instantaneous system demand

**Table 4**  
Comparison of SOFC subsystem performance to available benchmark cases.

	Case A (H <sub>2</sub> )		Case B (natural gas)	
	IEA	Model	IEA	Model
Voltage (V)	0.71	0.71	0.64	0.64
Current (A·m <sup>-2</sup> )	3000 avg	4203 avg	3000 avg	3712 avg
Power (W·m <sup>-2</sup> )	2130	2984	1923	2645
T <sub>anode</sub> (K)	1332 out	1293 avg 1332 out	1296 out	1258 avg 1295 out
T <sub>cathode</sub> (K)	1332 out	1280 avg 1328 out	1293 out	1247 avg 1293 out
T <sub>tri</sub> (K)	1336 max	1290 avg 1331 max	1298 max	1253 avg 1294 out
U <sub>f</sub>	0.85	0.85	N/A	0.85

and natural gas steam reformat (26.26% H<sub>2</sub>; 17% CH<sub>4</sub>; 49.34% H<sub>2</sub>O; 2.94%CO; 4.36% CO<sub>2</sub>) as the feed fuels, with inlet streams at 1173 K and 1 atm. The SOFC subsystem was therefore run with these same conditions, holding voltage at the average values provided in the report and attempting to use cathode flowrate to match the average value of key temperatures reported, as well. Table 4 compares the values reported in the IEA document to those obtained with the SOFC subsystem. As can be seen in the data, fuel utilization and temperature features are well-matched between the current and previous works. The only significant difference is in the current and power densities. However, this is expected as the electrochemical model utilized in this investigation is from a more modern cell's performance than those simulated in the previous work. Fig. 6 also provides a comparison between the IEA report's temperature and current density profiles and those obtained with the SOFC subsystem, for the H<sub>2</sub> case. Comparing the current model's data to those from the IEA report, it can be seen that key features, including local maxima and overall shapes of the trends are in good agreement. Note that the improved performance from the current model's electrochemistry is noticeable in that the current density does not drop as sharply along the length of the fuel cell channels, in spite of similar maximum values at the inlet of the fuel cell. Similar matches in trends were obtained in the natural gas case.

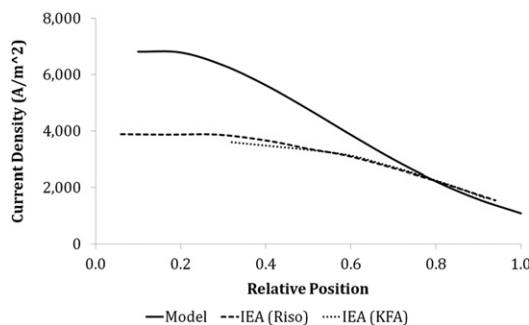


**Fig. 6.** Comparison of SOFC subsystem spatial trends to available benchmark case.

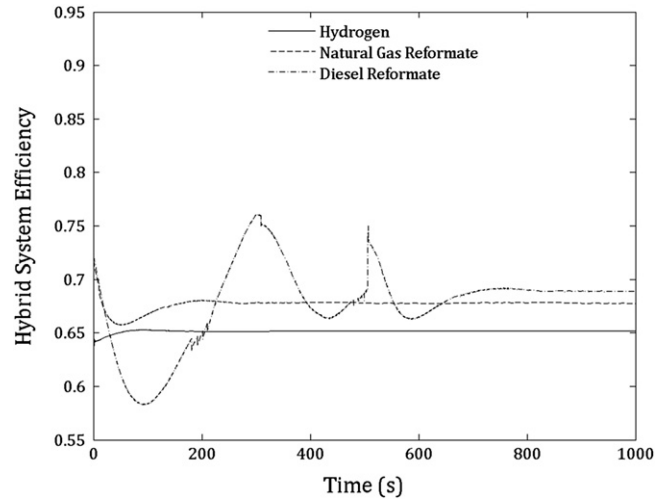


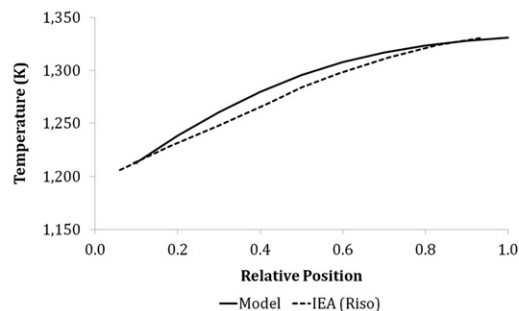
**Fig. 7.** System efficiency during transient convergence to steady state for all fuels.

### 3.2. Steady-state system design point simulations

With the SOFC subsystem verified, the performance of the entire hybrid system was then investigated, starting with the expected design point performance at rated power. The system was therefore initialized to a state near the desired design point and then controlled for an approach to steady-state. The target operating state for hydrogen and natural gas reformat was to achieve 3.5 MW total system power while maintaining an 85% anode fuel utilization, an average SOFC temperature of 1123 K, a temperature rise across the SOFC less than 200 K, and a combustor temperature between 1223 K and 1523 K. For the diesel reformat case, the fuel utilization constraint was reduced to 80% because the higher utilization was unsustainable for this fuel. Controller gains were tuned such that the performance could be reached in the steady-state simulation with reasonable transient characteristics; however, they were not optimized during this investigation. The fuel compositions for hydrogen and natural gas reformat have previously been described; for diesel reformat, the composition was 21.7% H<sub>2</sub>; 0.5% CH<sub>4</sub>; 17.8% H<sub>2</sub>O; 10% CO; 8.8% CO<sub>2</sub>; 41% N<sub>2</sub>. This composition is as observed from diesel autothermal pre-reformer studies reported in [38], which utilized synthetic diesel blends as surrogates for commercial diesel.

The development of the steady-state efficiencies for all three cases is shown in Fig. 7. In this work, the system efficiency presented is a fuel-to-electric efficiency defined as

$$\eta_{\text{Sys}} = \frac{P_{\text{SOFC}} + P_{\text{Turb}} - P_{\text{Blow}}}{\text{LHV}_{\text{SOFC+Turb}}} \quad (40)$$



where  $P_{\text{SOFC}}$ ,  $P_{\text{Turb}}$ , and  $P_{\text{Blow}}$  are the SOFC power, net turbine power (referred to as Load in the figures presented below), and the cathode recycle blower power;  $\text{LHV}_{\text{SOFC+Turb}}$  is the combined heating value from the flow of fuel into the SOFC anode channels and the auxiliary burner. All three systems achieve efficiency estimates greater than 65%, with the natural gas reformat and diesel reformat cases achieving slightly higher efficiencies than the hydrogen case. This trend in system efficiency was caused by a matching trend in the steady operating point of the turbine (82.1%, 82.6%, and 84.1% isentropic efficiency for hydrogen, natural gas, and diesel cases, respectively). The difference in component efficiency was caused by the combustor control method, which allowed turbine inlet temperature to acquire a range of values rather than holding all cases to a common value. Simulation results indicated temperatures of 1260 K, 1275 K, and 1330 K for hydrogen, natural gas, and diesel respectively. This temperature variation was caused by the lower SOFC fuel utilization in the diesel case, which allowed more fuel to be burned in the combustor, which is a greater thermal energy source than the SOFC. It should be emphasized that

the fuel reformat cases do not consider the energy requirements of fuel conversion; the impact of the associated energy requirements for this step will be discussed in Part 2 of this work.

For the hydrogen and natural gas cases, 1000 s was enough to come to steady state, but diesel required up to 10,000 s (not shown). Additionally, the hydrogen case was the most stable, with the natural gas reformat case exhibiting some small instabilities, possibly due to the competing action of electrochemical oxidation and reformation within the anode as well as longer times spent in higher levels of the control cascade, leading to longer settling times. Clearly, the diesel reformat case exhibited the most dramatic transient behavior, requiring long times to settle at a given level of the control cascade before proceeding to deeper levels.

Fig. 8 shows the dynamic response to control decisions for the diesel reformat case. Panels a through e display the development of the control and manipulated variables for control levels 1–4, respectively (panels d and e correspond to Level 4 together). Panel f displays the final species concentration development through the length of the cell at 10,000 s of run time. In panels a–d,

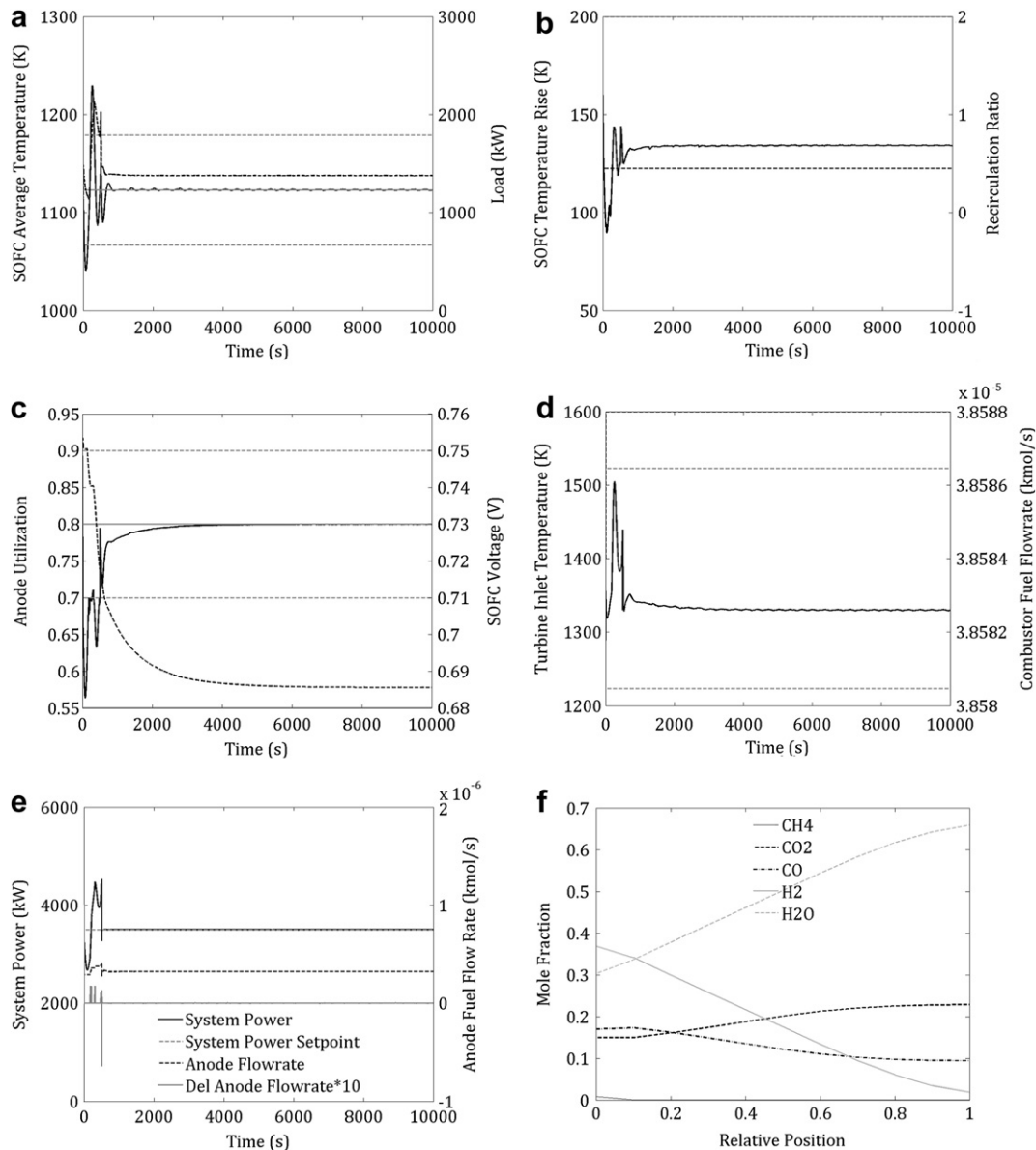


Fig. 8. Control actions and SOFC anode species mole fractions for diesel reformat case.

solid black lines represent the controlled variable on the primary axis, dashed black lines represent the manipulated variable on the secondary axis, solid gray lines indicate the target value for the controlled variable, and dashed gray lines indicate the desired bounds of the controlled variable. There are multiple instances through the initial transient response when the limits on average SOFC temperature were violated and the control methodology returned to this high level before addressing the other control variables. These divergences into unfavorable operation zones correspond to the initial reaction of the system when it enters a deeper level of the control cascade. For example, the first violation in SOFC average temperature comes shortly after the first drop in SOFC voltage to attempt to meet the utilization target. It can then be seen through comparison of panels a and c that the control of the anode utilization is momentarily halted while the load adjusts to meet the average SOFC temperature criterion. This is exhibited in panel c as a short, horizontal plateau in SOFC voltage between two major drops in that voltage.

Not surprisingly, during the times when control returned to Level 1, the anode utilization itself exceeded the bounds of its desired operation; thus, once control fell to this level again, then another change is made in SOFC voltage. As a result, there is a brief time of approximately 800 s where control seems to oscillate between Levels 1 and 3. Coincidentally, Level 2 and the turbine inlet temperature restriction in Level 4 are always within their limits during this time, therefore not requiring the attention of the controller. Finally, it can be seen that during these initial 800 seconds, the total system power is varying significantly around its setpoint; however, once Levels 1 and 3 were satisfied, coming to compliance on the total system power was both swift and apparently transparent to the higher control levels. Similar data were collected for the other fuel cases; however, the data shown in Fig. 8 are representative and exhibit more of the interplay between cascade levels in the controller than the data for the other fuel cases.

The need for the lower utilization target for the diesel case can be seen by close inspection of Fig. 7 and panels a–e of Fig. 8. Note

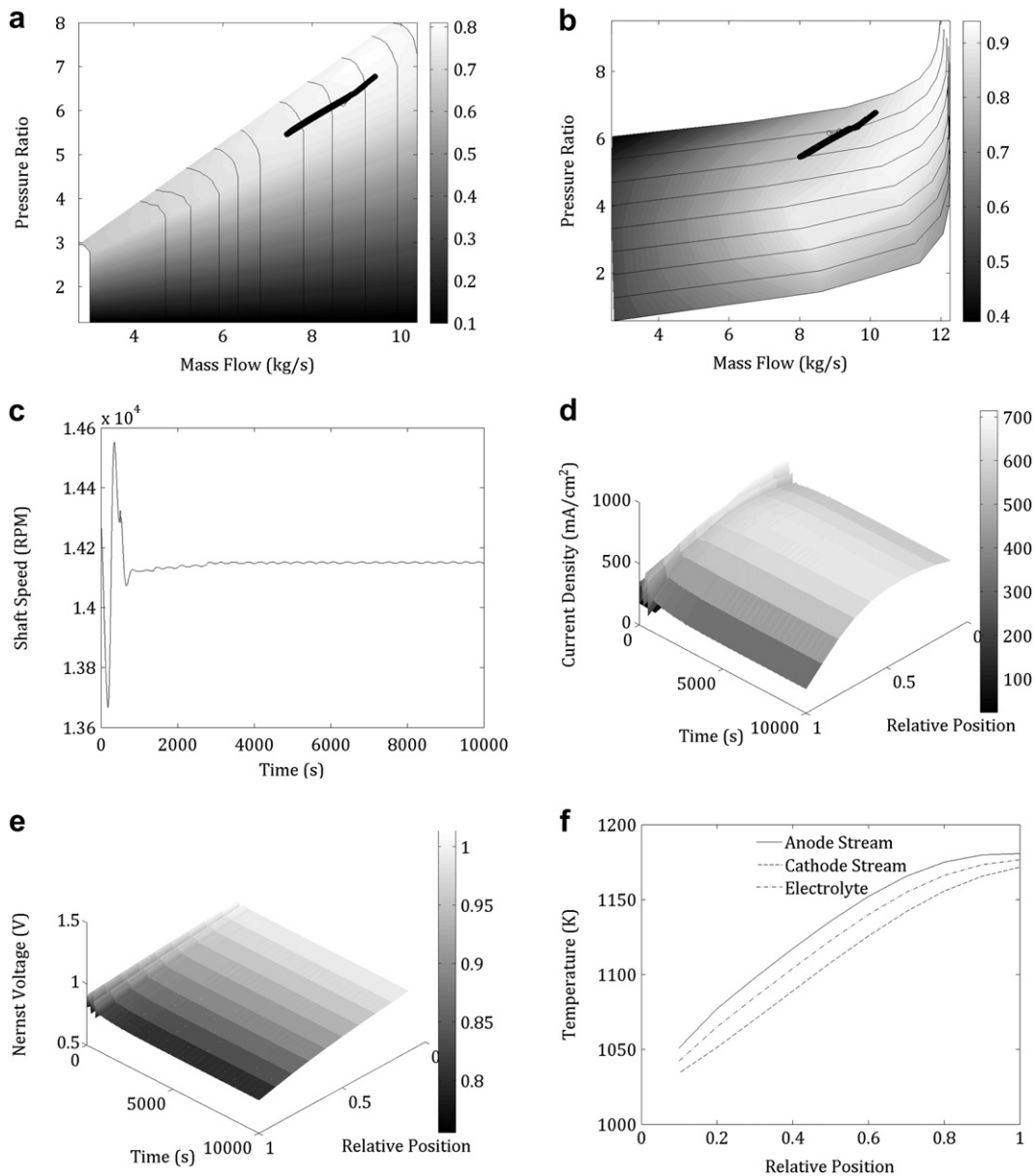


Fig. 9. System performance for diesel reformat case during development of steady state.

that the steady-state solutions exhibit a small amount of oscillation. When the diesel reformat case was originally run with a fuel utilization target of 85%, SOFC voltage would be pushed too far below the limits of operation. As a result, the control settled on a fuel utilization of 82% but very low system efficiency and an inability to meet system net power demand. It can therefore be surmised that anode fuel utilization in this case near 80% is most likely pushing the SOFC Subsystem to the limits of its operational range, imparting the observed instability on the resulting performance.

Panel f of Fig. 8 provides insight into the fundamental cause of this instability. All of the methane is consumed very close to the front of the SOFC anode channel, with almost all of the hydrogen consumed by the exit. For the case of a general fuel reformat stream, methane, hydrogen, and carbon monoxide must all be considered fuels. Carbon monoxide, much like methane, undergoes a reaction process (involving the water–gas shift reaction) within the anode channel that gives rise to the formation of fuel hydrogen. However, as shown in panel f, the water–gas shift reaction approaches equilibrium by the time the flow exits the cell, with a high concentration of CO. This large amount of remaining CO therefore limits the achievable utilization.

It would therefore be desirable to incorporate a reaction model that accounts for water–gas shift, hydrogen electrochemical oxidation, and carbon monoxide electrochemical oxidation in order to more accurately represent the limits of operation on the diesel reformat. However, as of the time of this publication's writing, the authors have not identified a suitably detailed mechanism that accounts for the intricacies of the competition between these reactions. Moreover, it is fairly standard practice in the literature to assume that CO only participates in the water–gas shift reaction. It should be noted that the natural gas reformat case did not exhibit this problem, most likely due to the much higher concentration of methane and lower concentration of carbon monoxide.

Fig. 9 provides detailed data regarding the operation of the individual power-producing components within the system for the diesel reformat case. Panels a through c present the general turbine subsystem performance, with the operating line during the transient overlaying the performance maps for the compressor and turbine, respectively in panels a and b and the shaft speed displayed in panel c. Using the compressor map as reference, the system was first put at a state near the efficiency island at the upper-right corner of the map. Progression from this point to the final steady state then followed a path of oscillation, indicated in panel c. Overall, the final steady-state operation was nearer to the efficiency island of both components than the initial state, with a pressure ratio of 6.1. Within the SOFC, the current density obtained a peak at approximately 40% of the total travel length within the channel, at 645 mA/cm<sup>2</sup>. Panels e and f show that Nernst voltage dropped along the length of the fuel cell, in agreement with the rising temperature in the same direction. Comparison to Fig. 8 shows current density closely followed average SOFC temperature and Nernst voltage closely followed the anode utilization.

Table 5 compares the final state for all three fuel cases. There is not much variation between the cases in the operation of the turbomachinery, with component efficiencies and shaft speed very

close to each other for all cases. Most of the variation appears to actually occur in the fuel cell itself, and most apparently in the voltage and the current density. The current density of the diesel reformat case is markedly lower than the other two cases, most likely due to previous observations regarding the inlet composition and the fact that carbon monoxide electrochemical oxidation is not accounted for in this model. In addition, the voltage of the hydrogen fuel case is significantly higher than the other two due to its much higher hydrogen inlet concentration. The natural gas reformat case comes close to the upper limit of temperature rise, possibly due to its high current density, which counteracts a large amount of the endothermic cooling provided by the internal reformation at the entrance of the cell.

### 3.3. Demonstrative system dynamic response

In order to investigate response to dynamically changing system demand, all three cases were initialized to their final states as shown in the previous steady-state results. This state was then held for an additional 1000 s before a 500 kW step in additional power demand was introduced to the controller logic. This power demand was maintained for 3000 s, followed by another step increase of 500 kW, another 3000 s holding period, a 1000 kW step decrease in power demand, and a final 3000 s holding period. In a manner similar to Fig. 7, Fig. 10 presents the system efficiency of the three fuel cases. As with the steady-state system results, the diesel reformat case consistently exhibited the highest system efficiency, with natural gas reformat very nearly matching the diesel reformat.

System efficiency closely tracked the step changes in demand after the settling of initial transients, with larger overshoots during load sheds than load additions. It can also be seen that the effect is most severe in the hydrogen case. The source of this is most likely thermal in nature. As the SOFC operates, its net thermal impact is a production of heat. Increases in power demand would require higher temperatures throughout the system, including the fuel cell. Since the fuel cell prefers to generate heat, the demand for extra heat to support the additional demand is in accordance with the operational characteristics of the SOFC. However, when the system needs to shed load, lower temperatures are required throughout the system; as the SOFC prefers to generate heat, rather than consume it, this is in odds with the fuel cell's operation. It therefore takes a longer time for the SOFC to

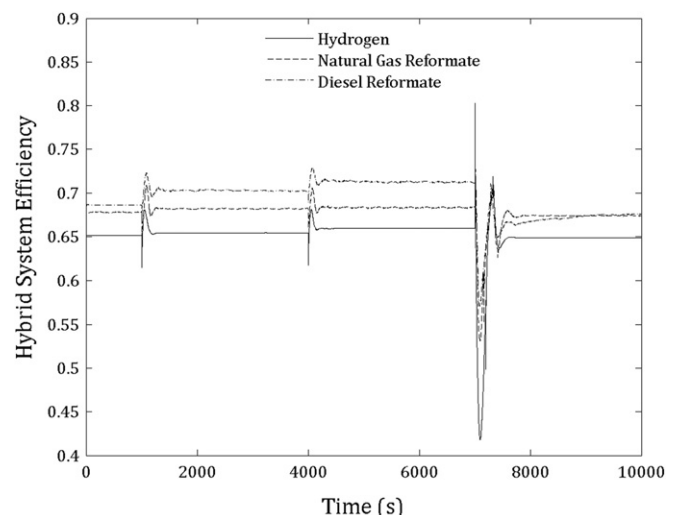


Fig. 10. Dynamic response of system efficiency for all modeled fuels.

Table 5  
Comparison of system performance when operated on all modeled fuels.

Fuel	$\eta_{\text{Turb}}$ (%)	$\eta_{\text{Comp}}$ (%)	$N_{\text{CT}}$ (RPM)	$j_{\text{Ave}}$ (mA-cm <sup>-2</sup> )	$V$ (V)	$\Delta T_{\text{SOFC}}$ (K)
Hydrogen	82.1	78.2	14,243	610.1	0.743	151.2
Natural gas reformat	82.6	77.1	14,007	662.4	0.677	187.3
Diesel reformat	84.1	77.7	14,149	523.9	0.686	134.1

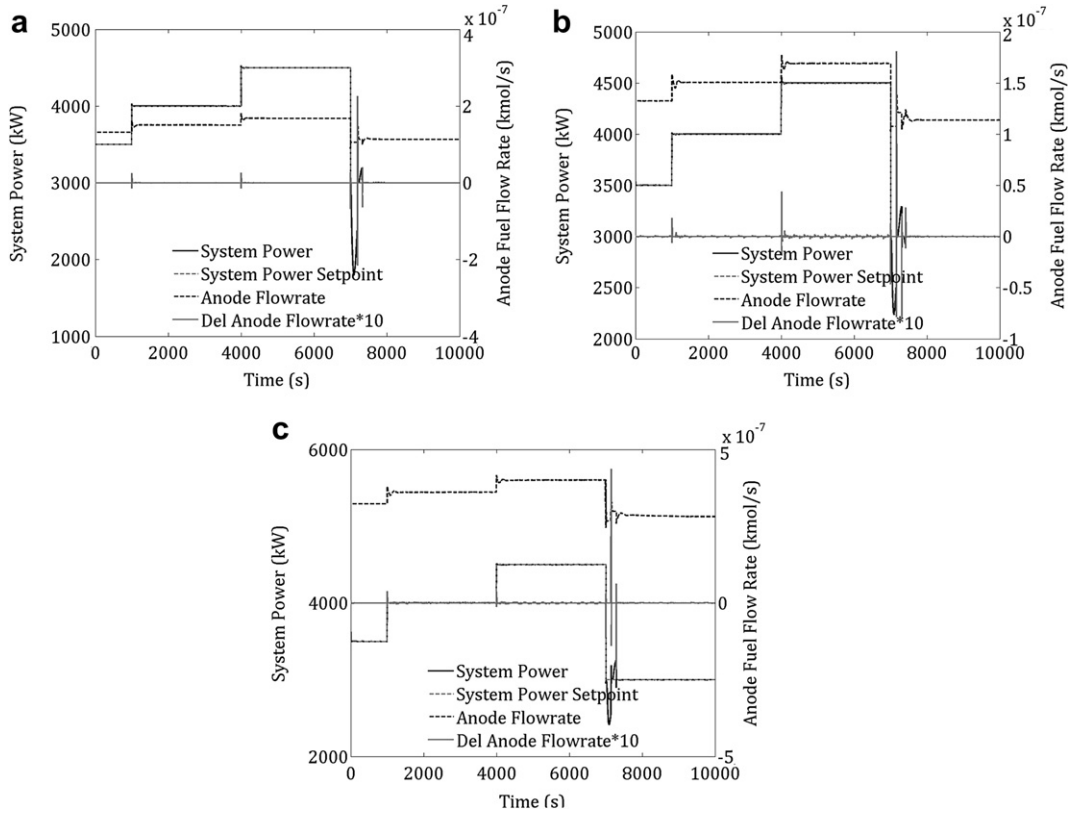


Fig. 11. Dynamic system performance during step load changes for (a) hydrogen, (b) natural gas reformat, and (c) diesel reformat.

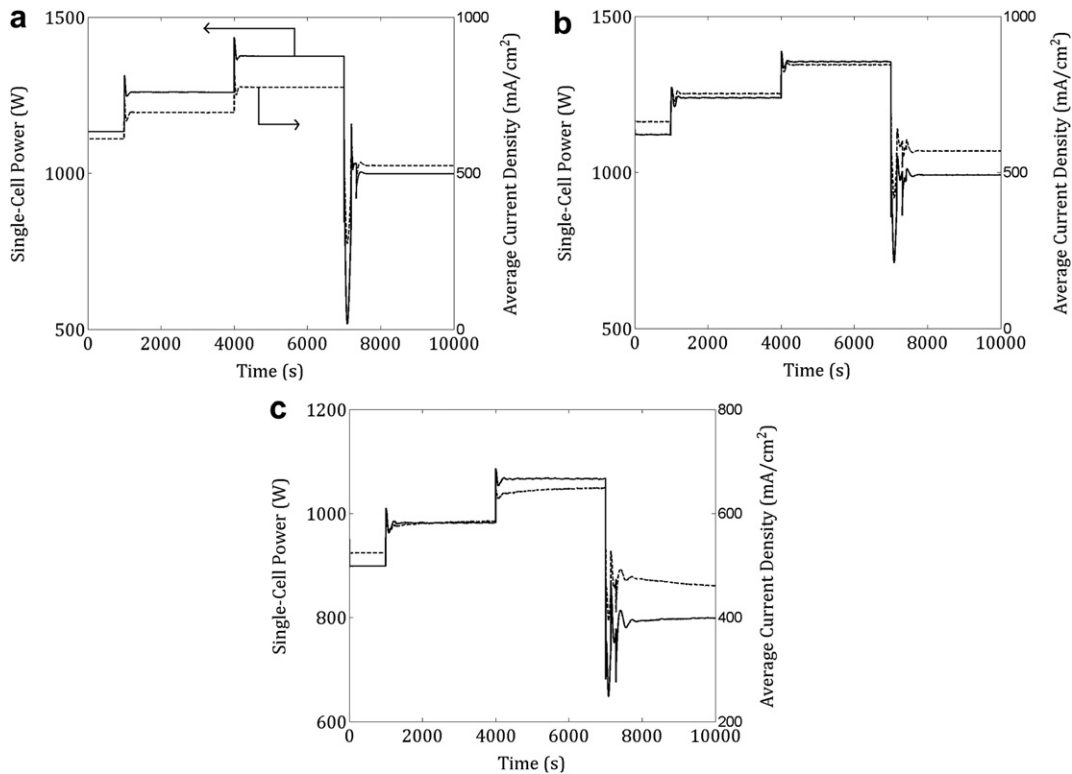


Fig. 12. Electrochemical dynamic response for (a) hydrogen, (b) natural gas reformat, and (c) diesel reformat.

adjust and the impact on the SOFC performance is greater since it requires greater changes in the manipulated variables utilized in control.

In addition, the impact can be expected to be greater for the hydrogen case since it does not include any endothermic reformation steps, which act as a thermal sink. Moreover, in the steady state, the diesel reformate case requires  $\sim 2.3$  times the fuel molar flowrate compared to the natural gas reformate case because the assumption of ATR in the diesel reformate case introduces a substantial amount of nitrogen into the stream, which acts as a significant diluent and heat sink.

Fig. 11 presents the developed system powers for all three cases during the transients. The hydrogen-fueled system responded the fastest, with the smallest overshoots. However, all three cases provide acceptable performance. The increased fuel feed requirement of the diesel reformate case is clearly apparent in Fig. 11, and it can be seen that for all three cases, the system is able to quickly respond to the change in demand by proceeding all the way to Level 4 of the control cascade. Upon the load additions, all three fuel cases can stay at this cascade level while maintaining compliance with the other control variables. However, upon the load shed, all three cases leave this control cascade level, as is exhibited by the brief horizontal plateaus in the Anode Flowrate trends. The natural gas case at first has the most trouble of the three fuels. However, investigation of both Figs. 10 and 11 show that hydrogen and natural gas are able to come to steady-state well before the end of the settling time for all three load changes. By contrast, the diesel reformate case is still approaching steady state at the end of simulation after the load shed (this is most apparent in Fig. 10).

The longer settling time for the diesel reformate case is an effect of the electrochemistry, and again tied to the difficulties observed in controlling the fuel utilization when operating on this fuel. Fig. 12 shows the electrochemical performance of all three cases, revealing that the average current density in the diesel reformate case is still settling out at the end of simulation, while the other two cases exhibit relative ease in coming to steady state. Fig. 13 shows the voltage of the cell for the diesel reformate case is nowhere near steady state at the end of simulation, and experiences a large transient after the load shed in an apparent attempt to bring the fuel utilization well under control. In fact, for all load changes, it can be seen that the fuel utilization in the diesel reformate case never really reaches its target value, and takes a long time in its approach to the target, with significant voltage changes driving this process. Although the settling time is long for the diesel reformate case, at

no time does the utilization exceed the bounds of its desired operation.

#### 4. Summary and conclusions

A model of a simplified SOFC-GT hybrid system with cathode-side recirculation and the capability to simulate dynamic performance as well as provide spatially resolved data within the SOFC channels has been successfully demonstrated. The goal of the model is to analyze the potential for a SOFC-GT system to provide the motive power in a diesel-power freight locomotive. The design of the system model has been built around this capability, with inclusion of subroutines that can incorporate even more detailed physics of diesel reformation and electrochemical oxidation of reformation products. Analysis of the system began by demonstrating that the performance of the SOFC subsystem matches well with the published performance of a benchmark model operating on both humidified hydrogen and natural gas reformate. Simulation of the system at its design point has shown promising results for a system operating on any one of three candidate fuels: hydrogen, natural gas reformate, and diesel reformate. Projected system efficiencies between 65% and 70% are in agreement with previous results in the literature when taking into account the fact that the model as presented does not account for the losses in the reformation of the hydrocarbon fuels themselves.

It was found that although all three fuels provide satisfactory performance and are roughly comparable at rated operation, the use of diesel fuel reformate imparts longer transients during dynamic power changes. This was shown to be related to the difficulty in accurately and quickly controlling the fuel utilization for this fuel. The model accounts for the large amount of nitrogen in diesel reformate (which acts as a diluent) as well as the large amounts of carbon monoxide provided in the inlet stream. This may lead to the need to critically evaluate the common assumption that CO does not participate electrochemically in a typical SOFC. This work indicates there may exist conditions within the cell at which all other reaction routes (hydrogen electrochemistry, reformation, and water-gas shift) are exhausted and CO electrochemical oxidation may become favored.

Part II of this work directly addresses the application of this system to the locomotive platform, concentrating on physical constraints as well as performance along a representative route in the South Coast Air Basin in California. Utilization of modeled train kinematics as well as physical characteristics of the representative route will allow for a more complete and thorough understanding of the dynamic response capability of the system than the simple representative dynamics investigated in this work. Future work will include system design alternatives, including reformer thermal integration. In addition, coke-related SOFC degradation studies will be carried out with the goal to better understand the system's ability to meet current service lifetime expectations, typically on the order of decades.

#### Acknowledgments

The authors gratefully acknowledge the funding support for this effort that was provided by the California Air Resources Board and the South Coast Air Quality Management District

The statements and conclusions in this Report are those of the contractor and not necessarily those of the California Air Resources Board. The mention of commercial products, their source, or their use in connection with material reported herein is not to be construed as actual or implied endorsement of such products.

This report was prepared as a result of work sponsored, paid for, in whole or in part, by the South Coast Air Quality Management

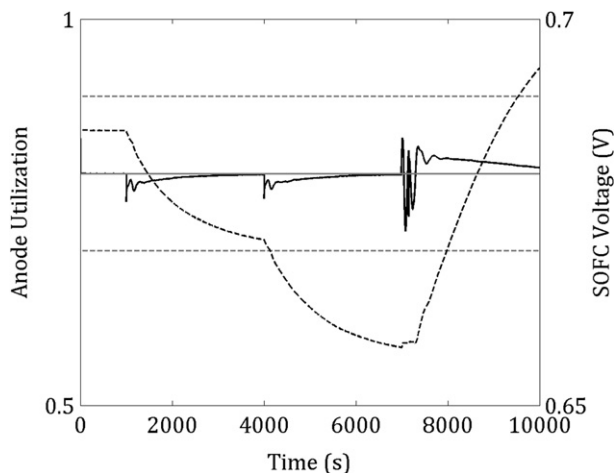


Fig. 13. Dynamic control response for voltage manipulation attempting to satisfy utilization constraints in the diesel reformate case.

AQMD (AQMD). The opinions, findings, conclusions, and recommendations are those of the author and do not necessarily represent the views of AQMD. AQMD, its officers, employees, contractors, and subcontractors make no warranty, expressed or implied, and assume no legal liability for the information in this report. AQMD has not approved or disapproved this report, nor has AQMD passed upon the accuracy or adequacy of the information contained herein.

## References

- [1] Frank Stodolsky, Railroad and Locomotive Technology Roadmap, US Department of Energy, Argonne, 2002.
- [2] S.C. Davis, S.W. Diegel, Transportation Energy Data Book: Edition 26, Oak Ridge National Laboratory, Oak Ridge, 2007.
- [3] H. Holmes, et al., Recommendations to Implement Further Locomotive and Railyard Emission Reductions, California Air Resources Board, 2009.
- [4] Diesel Particulate Matter Exposure Assessment Study for the Ports of Los Angeles and Long Beach, California Air Resources Board, Sacramento, 2006.
- [5] United States. Environmental Protection Agency, Control of emissions of air pollution from locomotive engines and marine compression-ignition engines less than 30 liters per cylinder; final rule, Federal Register 6 (May 2008) 25,098–25,146 Print.
- [6] R.A. Roberts, J. Brouwer, Dynamic simulation of a pressurized 220 kW solid oxide fuel–cell–gas-turbine hybrid system: modeled performance compared to measured results, *Journal of Fuel Cell Science and Technology* 3 (2006) 18–25.
- [7] Veyo, et al., Tubular solid oxide fuel cell/gas turbine hybrid cycle power systems: status, *Journal of Engineering for Gas Turbines Power* 124 (2002) 845–849.
- [8] B.A. Steinberg, D.S. Scott, Hydrogen vs diesel fueled locomotives: a techno-economic appraisal, *International Journal of Hydrogen Energy* 9 (1) (1984) 101–107.
- [9] L.E. Jones, et al., Fuel cell alternative for locomotive propulsion, *International Journal of Hydrogen Energy* 10 (7, 8) (1985) 505–516.
- [10] H.S. Murray, J.R. Huff, E.W. Gregory II, Fuel cell power plants for heavy-duty transportation applications, *Extended Abstracts of the Electrochemical Society* 82 (1982) 471.
- [11] D.S. Scott, H.H. Rogner, M.B. Scott, Fuel cell locomotives in Canada, *International Journal of Hydrogen Energy* 18 (3) (1993) 253–263.
- [12] M. Shimada, R. Furuta, J. Kawasaki, S. Takeda, T. Kaneko, E. Toyota, Trial run of fuel cell hybrid traction system for railcar. In: *Proceedings of the 23rd electric vehicle symposium, Anaheim* (2007).
- [13] H. Hasegawa, Y. Ohki, Development of a model of on-board PEMFC powered locomotive with a metal hydride cylinder, *Materials Research Society Symposium Proceedings* 393 (1995) 145–150.
- [14] G.D. Marin, G.F. Naterer, K. Gabriel, Rail transportation by hydrogen vs. electrification – case study for Ontario Canada, I: propulsion and storage, *International Journal of Hydrogen Energy* 35 (12) (2010) 6084–6096.
- [15] A.R. Miller, J. Peters, Fuel cell hybrid locomotives: applications and benefits. In: *Proceedings of the 2006 IEEE/ASME joint rail conference, Atlanta* (2006).
- [16] A.R. Miller, J. Peters, B.E. Smith, O.A. Velev, Analysis of fuel cell hybrid locomotives, *Journal of Power Sources* 157 (2006) 855–861.
- [17] A.R. Miller, K.S. Hess, D.L. Barnes, T.L. Erickson, System design of a large fuel cell hybrid locomotive, *Journal of Power Sources* 173 (2007) 935–942.
- [18] R. Roberts, et al., Control design of an atmospheric solid oxide fuel cell/gas turbine hybrid system: variable versus fixed speed gas turbine operation, *Journal of Power Sources* 161 (2006) 484–491.
- [19] F. Mueller, et al., Synergistic integration of a gas turbine and solid oxide fuel cell for improved transient capability, *Journal of Power Sources* 176 (2008) 229–239.
- [20] P. Costamagna, L. Magistri, A.F. Massardo, Design of a hybrid system based on a solid oxide fuel cell reactor and a micro gas turbine, *Journal of Power Sources* 96 (2001) 352–368.
- [21] L. Magistri, et al., Design and off-design analysis of a MW hybrid system based on rolls-royce integrated planar solid oxide fuel cells, *Journal of Fuel Cell Science and Technology* 129 (2007) 792–797.
- [22] C. Bao, et al., Multi-level simulation platform of SOFC-GT hybrid generation system, *International Journal of Hydrogen Energy* 35 (2008) 2894–2899.
- [23] J.S. Yang, J.L. Sohn, S.T. Ro, Performance characteristics of a solid oxide fuel cell/gas turbine hybrid system with various part-load control modes, *Journal of Power Sources* 166 (2007) 155–164.
- [24] T. Kaneko, J. Brouwer, G.S. Samuelsen, Power and temperature control of fluctuating biomass gas fueled solid oxide fuel cell and micro gas turbine hybrid system, *Journal of Power Sources* 160 (2006) 316–325.
- [25] X.-J. Wu, Q. Huang, X.-J. Zhu, Thermal modeling of a solid oxide fuel cell and micro gas turbine hybrid power system based on modified LS-SVM, *International Journal of Hydrogen Energy* 36 (2011) 885–892.
- [26] C. Stiller, et al., Control strategy for a solid oxide fuel cell and gas turbine hybrid system, *Journal of Power Sources* 158 (2006) 303–315.
- [27] Y. Li, Y. Weng, Performance study of a solid oxide fuel cell and gas turbine system designed for methane operating with non-designed fuels, *Journal of Power Sources* 196 (2011) 3824–3835.
- [28] M. Li, A.D. Rao, J. Brouwer, G.S. Samuelsen, Design of highly efficient coal-based integrated gasification fuel cell power plants, *Journal of Power Sources* 195 (2010) 5707–5718.
- [29] E. Bompard, et al., Technical considerations of SOFCs for mixed DG/backup power applications, *International Journal of Hydrogen Energy* 33 (2008) 6743–6748.
- [30] S. Krumdieck, S. Page, S. Round, Solid oxide fuel cell architecture and system design for secure power on an unstable grid, *Journal of Power Sources* 125 (2004) 189–198.
- [31] W. Winkler, H. Lorenz, Design studies of mobile applications with SOFC-heat engine modules, *Journal of Power Sources* 106 (2002) 338–343.
- [32] L. Tse, et al., Solid oxide fuel cell/gas turbine trigeneration system for marine applications, *Journal of Power Sources* 196 (2011) 3149–3162.
- [33] G. Sattler, Fuel cells going on-board, *Journal of Power Sources* 86 (2000) 61–67.
- [34] P. Costamagna, et al., Electrochemical model of the integrated planar solid oxide fuel cell (IP-SOFC), *Chemical Engineering Journal* 102 (2004) 61–69.
- [35] Frank P. Incropera, David P. De Witt, in: *Fundamental of heat and mass transfer*, 5th ed. John Wiley & Sons, Hoboken, 2002.
- [36] Solar turbines, Solar 20 gas turbine generator set (2005).
- [37] E. Achenbach, SOFC stack modeling, final report of activity A2, annex II: modeling and evaluation of advanced solid oxide fuel cells. IEA Programme on R, D&D on Advanced Fuel Cells, Juelich, Germany (1996).
- [38] I. Kang, Y. Kang, S. Yoon, G. Bae, J. Bae, The operating characteristics of solid oxide fuel cells driven by diesel autothermal reformat, *International Journal of Hydrogen Energy* 33 (21) (2008) 6298–6307.